Improving thermodynamic profile retrievals from microwave radiometers by including Radio Acoustic Sounding System (RASS) observations

Irina V. Djalalova[1,2], David D. Turner[3], Laura Bianco[1,2],

James M. Wilczak[2], James Duncan[1,2*], Bianca Adler[1,2] and Daniel Gottas[2]

[1] Cooperative Institute for Research in Environmental Sciences (CIRES), Boulder, CO, USA

[2] National Oceanic and Atmospheric Administration, Physical Sciences Laboratory, Boulder, CO, USA

[3] National Oceanic and Atmospheric Administration, Global Systems Laboratory, Boulder, CO USA

[*]Now at WindESCo, Burlington, MA

Corresponding author address: Irina V. Djalalova (Irina.V.Djalalova@noaa.gov), NOAA/Physical Science Laboratory, 325 Broadway, mail stop: PSD3, Boulder, CO 80305. Tel.: 303-497-6238. Fax: 303-497-6181.

22 **Outline**

23 **Abstract**

24 **1. Introduction**

25 **2. XPIA dataset**

26 **2.1 MWR measurements**

27 **2.2 WPR-RASS measurements**

28 **2.3 BAO data**

29 **2.4 Radiosonde measurements**

30 **3. Physical retrievals**

31 **3.1 Iterative retrieval technique**

32 **3.2 Bias-correction of MWR observations using radiosondes or climatology**

33 **3.3 Analysis of physical retrieval characteristics**

34 **4. Results**

35 **4.1 Statistical analysis of the physical retrievals up to 3 km AGL**

36 **4.2 Statistics for the profiles least close to the climatology**

37 **4.3 Virtual temperature statistics**

38 **5. Conclusions**

39 **Appendix A**

40 **Data availability**

41 **Author contribution**

42 **Acknowledgments**

43 **References**

Abstract

Thermodynamic profiles are often retrieved from the multi-wavelength brightness temperature observations made by microwave radiometers (MWRs) using regression methods (linear, quadratic approaches), artificial intelligence (neural networks), or physical-iterative methods. Regression and neural network methods are tuned to mean conditions derived from a climatological dataset of thermodynamic profiles collected nearby. In contrast, physical-iterative retrievals use a radiative transfer model starting from a climatologically reasonable profile of temperature and water vapor, with the model running iteratively until the derived brightness temperatures match those observed by the MWR within a specified uncertainty.

In this study, a physical-iterative approach is used to retrieve temperature and humidity profiles from data collected during XPIA (eXperimental Planetary boundary layer Instrument Assessment), a field campaign held from March to May 2015 at NOAA's Boulder Atmospheric Observatory (BAO) facility. During the campaign, several passive and active remote sensing instruments as well as in-situ platforms were deployed and evaluated to determine their suitability for the verification and validation of meteorological processes. Among the deployed remote sensing instruments were a multi-channel MWR, as well as two radio acoustic sounding systems (RASS), associated with 915-MHz and 449-MHz wind profiling radars.

In this study the physical-iterative approach is tested with different observational inputs: first using data from surface sensors and the MWR in different configurations, and then including data from the RASS into the retrieval with the MWR data. These temperature retrievals are assessed against co-located radiosonde profiles. Results show that the combination of the MWR and RASS observations in the retrieval allows for a more accurate

characterization of low-level temperature inversions, and that these retrieved temperature profiles match the radiosonde observations better than the temperature profiles retrieved from only the MWR in the layer between the surface and 3 km above ground level (AGL). Specifically, in this layer of the atmosphere, both root mean square errors and standard deviations of the difference between radiosonde and retrievals that combine MWR and RASS are improved by mostly 10-20% compared to the configuration that does not include RASS observations. Pearson correlation coefficients are also improved.

A comparison of the temperature physical retrievals to the manufacturer-provided neural network retrievals is provided in Appendix A.

1. Introduction

Monitoring the state of the atmosphere for process understanding and for model verification and validation requires observations from a variety of instruments, each one having its set of advantages and disadvantages. Using several diverse instruments allows one to monitor different aspects of the atmosphere, while combining them in an optimized synergetic approach can improve the accuracy of the information available on the state of the atmosphere.

During the eXperimental Planetary boundary layer Instrumentation Assessment (XPIA) campaign, a U.S. Department of Energy sponsored experiment held at the Boulder Atmospheric Observatory (BAO) in Spring 2015, several instruments were deployed (Lundquist et al., 2017) with the goal of assessing their capability for measuring atmospheric boundary layer meteorological variables. XPIA investigated novel measurement approaches, and quantified uncertainties associated with these measurement methods. While the main interest of the XPIA campaign was on wind and turbulence, measurements of other important atmospheric variables were also collected, including temperature and humidity. Among the deployed instruments were two identical microwave radiometers (MWRs) and two radio acoustic sounding systems (RASS), as well as radiosondes launches.

MWRs are passive sensors, sensitive to atmospheric temperature, humidity and liquid water path (LWP), that allow for a high temporal observation of the state of the atmosphere, with some advantages and limitations. In order to estimate profiles of temperature and humidity from the observed brightness temperatures (Tb), several methods could be applied such as regressions, neural network retrievals, or physical retrieval methodologies which can

include additional information about the atmospheric state in the retrieval process (e.g., Maahn et al. 2020). Microwave radiative transfer models (e.g., Rosenkranz, 1998; Clough et al. 2005) are commonly used to train statistical retrievals, or as forward models used within physical retrieval methods. Advantages of MWRs include their compact design, the relatively high temporal resolution of the measurements (2-3 minutes), the possibility to observe the vertical structure of both temperature and moisture through the lower part of the troposphere during both clear and cloudy conditions, and their capability to operate in a standalone mode. Disadvantages include limited accuracy in the presence of rain, rather coarse vertical resolution, and the necessity to have a site-specific climatology for retrievals. Other disadvantages include the challenges related to performing accurate calibrations (Küchler et al., 2016, and references within), radio frequency interference (RFI), and the low accuracy on the retrieved LWP especially for values of LWP less than 20 g m^{-2} (Turner 2007).

RASS, in comparison, are active instruments that emit a longitudinal acoustic wave upward, causing a local compression and rarefaction of the ambient air. These density variations are tracked by the Doppler radar associated with the RASS, and the speed of the propagating sound wave is measured. The speed of sound is related to the virtual temperature (Tv) (North et al., 1973), and therefore, RASS are used to remotely measure vertical profiles of virtual temperature in the boundary layer. Being an active instrument, the RASS is in general more accurate than a passive instrument (Bianco et al., 2017), but they also come with their own disadvantages. The main limitations of RASS for temperature measurements are the low temporal resolution (typically a 5-min averaged RASS profile is measured once or twice per hour), their limited altitude coverage, and the noise “pollution” that impacts local communities.

132 Adachi and Hashiguchi (2019) have shown that RASS could use parametric speakers to take
133 advantage of their high directivity and very low side lobes. Nevertheless, the maximum height
134 reached by the RASS is limited by sound attenuation, which is a function of both radar
135 frequency and atmospheric conditions (May and Wilczak, 1993) such as temperature, humidity,
136 and the advection of the propagating sound wave out of the radar's field-of-view. Therefore,
137 data availability is usually limited to the lowest several kilometers, depending on the frequency
138 of the radar. In addition, wintertime coverage is usually lower than that in summer, due to
139 increased attenuation of the acoustic signal in cooler and drier environments.

140 To get a better picture of the state of the temperature and moisture structure of the
141 atmosphere, it makes sense to try to combine the information obtained by both MWR and
142 RASS. Integration of different instruments has been and still is a topic of ongoing scientific
143 interest (Han and Westwater 1995; Stankov et al. 1996; Bianco et al., 2005; Engelbart et al.,
144 2009; Cimini et al., 2020; Turner and Löhnert, 2021, to name some). In this study, the focus is
145 on the combination of the MWR and RASS observations in the retrievals to improve the
146 accuracy of the temperature profiles in the lowest 3 km compared to physical retrieval
147 approaches that do not include the information from RASS measurements. Some studies have
148 used analyses from numerical weather prediction (NWP) models as an additional constraint in
149 these variational retrievals (e.g., Hewison 2007; Cimini et al. 2006, 2011; Martinet et al. 2020);
150 however, we have elected not to include model data in this study because we wanted to
151 evaluate the impact of the RASS profiles on the retrievals from a purely observational
152 perspective.

153 This paper is organized as follows: Section 2 summarizes the experimental dataset;
154 Section 3 introduces the principles of the physical retrieval approaches used to obtain vertical
155 profiles of the desired variables; Section 4 produces statistical analysis of the comparison
156 between the different retrieval approaches and radiosonde measurement; finally, conclusions
157 are presented in Section 5.
158

159 **2. XPIA dataset**

160 The data used in our analysis were collected during the XPIA experiment, held in Spring
161 2015 (March-May) at NOAA's BAO site, in Erie, Colorado (Lat.: 40.0451 N, Lon.: 105.0057 W, El.:
162 1584 m MSL). XPIA was the last experiment conducted at this facility, as after almost 40 years
163 of operations the BAO 300-m tower was demolished at the end of 2016 (Wolfe and Lataitis,
164 2018). XPIA was designed to assess the capability of different remote sensing instruments for
165 quantifying boundary layer structure, and was a preliminary study as many of these same
166 instruments were later deployed, among other campaigns, for the second Wind Forecast
167 Improvement Project WFIP2 (Shaw et al., 2019; Wilczak et al., 2019) which investigated flows in
168 complex terrain for wind energy applications, where they were for example used to study cold
169 air pools (Adler et al., 2021) and gap flow characteristics (Neiman et al., 2019; Banta et al.,
170 2020). The list of the deployed instruments included active and passive remote-sensing devices,
171 and in-situ instruments mounted on the BAO tower. Data collected during XPIA are publicly
172 available at https://a2e.energy.gov/projects/xpia. A detailed description of the XPIA
173 experiment can be found in Lundquist et al. (2017), while a specific look at the accuracy of the
174 instruments used in this study can be found in Bianco et al. (2017).

175

176 **2.1 MWR measurements**

177 Two identical MWRs (Radiometrics MP-3000A) managed by NOAA (MWR-NOAA) and by
178 the University of Colorado (MWR-CU), were deployed next to each other at the visitor center
179 ~600 m south of the BAO tower (see Lundquist et al., 2017 for a detailed map of the study
180 area). Prior to the experiment, both MWRs were thoroughly serviced (sensor cleaning, radome
181 replacement, etc.) and calibrated using an external liquid nitrogen target and an internal
182 ambient target. MWRs are passive devices which record the natural microwave emission in the
183 water vapor and oxygen absorption bands from the atmosphere, providing measurements of
184 the brightness temperatures. Both MWRs have 35-channels spanning a range of frequencies,
185 with 21 channels in the lower (22-30 GHz) K-band frequency band, of which 8 channels were
186 used during XPIA: 22.234, 22.5, 23.034, 23.834, 25, 26.234, 28 and 30 GHz; and 14 channels in
187 the higher (51-59 GHz) V-band frequency band, of which all were used in XPIA: 51.248, 51.76,
188 52.28, 52.804, 53.336, 53.848, 54.4, 54.94, 55.5, 56.02, 56.66, 57.288, 57.964 and 58.8 GHz.
189 Frequencies in the K-band are more sensitive to water vapor and cloud liquid water, while
190 frequencies in the V-band are sensitive to atmospheric temperature due to the absorption of
191 atmospheric oxygen (Cadeddu et al., 2013). V-band frequencies or channels can also be divided
192 in two categories: the opaque channels, 56.66 GHz and higher, that are more informative in the
193 layer of the atmosphere from the surface to ~1 km AGL, and the transparent channels, 51-56
194 GHz, that are more informative above 1 km AGL. Both MWRs observed at the zenith and at 15-
195 and 165-degree elevation angles in the north-south plane (referred to as oblique elevation
196 scans and used as their average hereafter; note zenith views have a 90-degree elevation angle).

197 However, when MWRs are deployed in locations with unobstructed views, oblique scans can be
198 performed down to 5 degrees elevation angles and may provide better temperature profile
199 accuracy in the lowest 0-1 or even 0-2 km AGL layers (Crewell and Löhnert, 2007).

200 In addition, each MWR was provided with a separate surface sensor to measure
201 pressure, temperature, and relative humidity at the installation level that was ~2.5 m AGL.
202 Vertical profiles of temperature (T), water vapor density (WVD), and relative humidity (RH)
203 were retrieved in real-time during XPIA every 2-3 minutes using a neural network (NN)
204 approach provided by the manufacturer of the radiometer (Solheim et al. 1998a, and 1998b;
205 Ware et al., 2003). Although the physical retrieval configurations used in this study do not
206 exactly match the NN retrieval configurations, a comparison of both physical and neural
207 network retrievals to the radiosonde temperature data is presented in Appendix A.

208 Both MWRs nominally operated from 9 March to 7 May 2015, although the MWR-NOAA
209 was unavailable between 5-27 April 2015. For the overlapping dates, temperature profiles
210 retrieved from the two MWRs showed very good agreement with less than 0.5 ^{o}C bias and
211 0.994 correlation (Bianco et al., 2017). For this reason, and because the MWR-CU was available
212 for a longer time period, only the MWR-CU (hereafter simply called MWR) is used.

213

214 **2.2 WPR-RASS measurements**

215 Two NOAA wind profiling radars (WPRs), operating at frequencies of 915-MHz and 449-
216 MHz, were deployed at the visitor center (same location as the MWR) during XPIA. These
217 systems are primarily designed to measure the vertical profile of the horizontal wind vector, but
218 co-located RASS also enable the observation of profiles of virtual temperature in the lower

atmosphere, with different resolutions and height coverages depending on the WPR. Thus, the RASS associated with the 915-MHz WPR (hereafter referred to as RASS 915) measured virtual temperature from 120 to 1618 m with a vertical resolution of 62 m, and the 449 MHz RASS (hereafter referred to as RASS 449) sampled the boundary layer from 217 to 2001 m with a vertical resolution of 105 m. The maximum height reached by the RASS is a function of both radar frequency and atmospheric conditions (May and Wilczak, 1993), and is usually lower for RASS 915 data, as will be shown later in the analysis.

The RASS data were processed using a radio frequency interference (RFI)-removal algorithm (performed on the RASS spectra), a consensus algorithm (Strauch et al. 1984) performed on the moment data using a 60% consensus threshold, a Weber-Wuertz outlier removal algorithm (Weber et al., 1993) performed on the consensus averages, and a RASS range-correction algorithm (Görsdorf and Lehmann, 2000) using an average relative humidity setting of 50% determined from the available observations.

2.3 BAO data

The BAO 300-m tower was built in 1977 to study the planetary boundary layer (Kaimal and Gaynor 1983). During XPIA, measurements were collected at the surface (2 m) and at six higher levels (50, 100, 150, 200, 250 and 300 m AGL). Each tower level was equipped with 2 sonic anemometers on orthogonal booms, and one sensor based on a Sensiron SHT75 solid-state sensor to measure temperature and relative humidity with a time resolution of 1 s, and averaged over five minutes. The more accurate temperature and water vapor observations

240 (Horst et al., 2016) at the BAO tower 2 m AGL level are used in the physical retrieval in place of
241 the less accurate MWR surface sensor.
242
243 **2.4 Radiosonde measurements**
244 Between 9 March and 7 May 2015, while the MWR was operational, radiosondes were
245 launched by the National Center for Atmospheric Research (NCAR) assisted by several students
246 from the University of Colorado over three selected periods, one each in March, April, and May.
247 All radiosondes were Vaisala model RS92. There was a total of 59 launches, mostly four times
248 per day, around 1400, 1800, 2200, and 0200 UTC (0800, 1200, 1600 and 2000 local standard
249 time, LST). The first 35 launches, between 9-19 March, were done from the visitor center, while
250 11 launches between 15-22 April, and 13 launches between 1-4 May, were done from the
251 water tank site, ~1000 meters away from the visitor center (see Lundquist et al., 2017 for a
252 detailed map of the study area). The radiosonde measurements included temperature, dew
253 point temperature, and relative humidity to altitudes usually higher than 10 km AGL, with
254 measurements every few seconds. As a first step, for additional verification, the radiosonde
255 data from the 59 launches taken between 9 March and 4 May 2015 were compared to the BAO
256 tower measurements, up to 300 m AGL. These observed data sets match very well, with a
257 correlation coefficient of 0.99 and a standard deviation of ~0.7 ^{o}C. However, one radiosonde
258 profile showed a large bias (> 5 ^{o}C) against all seven levels of BAO temperature measurements
259 and all available Tv measurements from the RASS 915 (eight measurements up to 600 m AGL)
260 and from the RASS 449 (nine measurements up to 1100 m AGL), therefore this particular
261 radiosonde profile was excluded from the statistical analysis. Moreover, while accurate RASS

data can be collected during rain, MWR data could be potentially deteriorated due to water deposition on the radome. Therefore, six profiles (three for March 13, and one each on May 1, 3 and 4) were eliminated from the statistical evaluation. These restrictions lowered the number of total radiosonde launches used in this study to 52.

3. Physical retrievals

One way to combine the active and passive instruments would be to use the RASS observations up to their maximum available height, and stitch them with the profiles obtained from a physical-iterative method using MWR data. To do this, the moisture contribution to the RASS virtual temperatures could be removed by using either the relative humidity measured by the MWR or by a climatology of the moisture term. However, merging these different profiles could result in artificial jumps at the connecting heights.

Alternatively, a physical retrieval (PR) iterative approach can be used to retrieve vertical profiles of thermodynamic properties from the MWR and RASS observations in a synergistic manner (e.g., Maahn et al 2020; Turner and Löhnert 2021). In this case, an optimal estimation-based physical retrieval is initialized with a climatologically reasonable profile of temperature and water vapor, and is iteratively repeated until the computed brightness temperatures match those observed by the MWR within the uncertainty of the observed brightness temperatures and the RASS virtual temperatures within their uncertainties (Rodgers, 2000; Turner and Löhnert, 2014; Cimini et al. 2018; Maahn et al. 2020).

3.1 Iterative retrieval technique

For this study, the PR uses the *TROPoe* retrieval algorithm (formerly *AERIoe*, Turner and Löhnert 2014; Turner and Blumberg 2019; Turner and Löhnert 2021). This algorithm is able to use radiance data from microwave radiometers, infrared spectrometers, and other observations as input. The microwave radiative transfer model, MonoRTM (Clough et al., 2005), serves as the forward model, which is fully functional for the microwave region and was intensively evaluated previously on MWR measurements (Payne et al. 2008; 2011).

We start with the state vector $\mathbf{X_a} = [\mathbf{T, Q,}\ \mathrm{LWP}]^T$, where superscript T denotes transpose, and vectors and matrices are shown in bold. **T** (K) and **Q** (g kg^{-1}) are temperature and water vapor mixing ratio profiles at 55 vertical levels from the surface up to 17 km, with the distance between the levels increasing geometrically with height. LWP is the liquid water path in (g m^{-2}) that measures the integrated content of liquid water in the entire vertical column above the MWR, and is a scalar. For this study, $\mathbf{X_a}$ has dimensions equal to 111 x 1 (two vectors **T** and **Q** with 55 levels each, and LWP). The retrieval framework of Turner and Blumberg (2019) is used, but only using MWR data (no spectral infrared). Here, we demonstrate the extension of the retrieval to include RASS profiles of **Tv**, and the resulting impact this has on the retrieved temperature profiles and information content.

The observation vector **Y** includes temperature and water vapor mixing ratio measured at the surface in-situ, and spectral **Tb** measured by the MWR. The MonoRTM model **F** is used as the forward model from the current state vector **X**, and is then compared to the observation vector **Y,** iterating until the difference between **F(X)** and **Y** is small within a specified uncertainty (Eq 1).

$$\boldsymbol{X_{n+1} = X_n + (S_a^{-1} + K^T S_\varepsilon^{-1} K)^{-1} K^T S_\varepsilon^{-1} [Y - F(X_n) + K(X_n - X_a)]} \quad (1)$$

307 with

308 $$X_a = \begin{bmatrix} \boldsymbol{T} \\ \boldsymbol{Q} \\ LWP \end{bmatrix} \qquad S_a = \begin{bmatrix} \boldsymbol{\sigma_{TT}^2} & \boldsymbol{\sigma_{TQ}^2} & 0 \\ \boldsymbol{\sigma_{QT}^2} & \boldsymbol{\sigma_{QQ}^2} & 0 \\ 0 & 0 & \sigma_{LWP}^2 \end{bmatrix} \qquad \boldsymbol{K_{ij} = \partial F_i / \partial X_j}$$

309 where i and j in the $\mathbf{K}_{ij}$ definition mark channel and vertical level, respectively. The superscripts

310 T and -1 in (1) indicate the transpose and inverse matrix, respectively. The observation vector **Y**

311 and the covariance matrix of the observed data, $\mathbf{S}_\varepsilon$, depending on the configuration used, are

312 equal to:

313 $$Y_1 = \begin{bmatrix} T_{sfc} \\ Q_{sfc} \\ \boldsymbol{Tb_{zenith}} \end{bmatrix} \qquad S_{\varepsilon_1} = \begin{bmatrix} \sigma_{Tsfc}^2 & 0 & 0 \\ 0 & \sigma_{Qsfc}^2 & 0 \\ 0 & 0 & \boldsymbol{\sigma_{Tb_{zenith}}^2} \end{bmatrix}$$

314 $$Y_2 = \begin{bmatrix} T_{sfc} \\ Q_{sfc} \\ \boldsymbol{Tb_{zenith+oblique}} \end{bmatrix} \qquad S_{\varepsilon_2} = \begin{bmatrix} \sigma_{Tsfc}^2 & 0 & 0 \\ 0 & \sigma_{Qsfc}^2 & 0 \\ 0 & 0 & \boldsymbol{\sigma_{Tb_{zenith+oblique}}^2} \end{bmatrix}$$

315 $$Y_3 = \begin{bmatrix} T_{sfc} \\ Q_{sfc} \\ \boldsymbol{Tb_{zenith+oblique}} \\ \boldsymbol{Tv_{RASS915}} \end{bmatrix} \qquad S_{\varepsilon_3} = \begin{bmatrix} \sigma_{Tsfc}^2 & 0 & 0 & 0 \\ 0 & \sigma_{Qsfc}^2 & 0 & 0 \\ 0 & 0 & \boldsymbol{\sigma_{Tb_{zenith+oblique}}^2} & 0 \\ 0 & 0 & 0 & \boldsymbol{\sigma_{Tv_{RASS915}}^2} \end{bmatrix}$$

316 $$Y_4 = \begin{bmatrix} T_{sfc} \\ Q_{sfc} \\ \boldsymbol{Tb_{zenith+oblique}} \\ \boldsymbol{Tv_{RASS449}} \end{bmatrix} \qquad S_{\varepsilon_4} = \begin{bmatrix} \sigma_{Tsfc}^2 & 0 & 0 & 0 \\ 0 & \sigma_{Qsfc}^2 & 0 & 0 \\ 0 & 0 & \boldsymbol{\sigma_{Tb_{zenith+oblique}}^2} & 0 \\ 0 & 0 & 0 & \boldsymbol{\sigma_{Tv_{RASS449}}^2} \end{bmatrix}$$

317 Note that the 2-m surface-level observations of temperature and water vapor mixing
318 ratio (T_{sfc} and Q_{sfc}, respectively) are included as part of the observation vector **Y**, and thus the
319 uncertainties (0.5 K for temperature and less than 0.4 g kg^{-1} for mixing ratio) in these
320 observations are included in $\mathbf{S_\epsilon}$.
321 The mean state vector of the climatological estimates, or a "prior" vector $\mathbf{X_a}$, is a key
322 component in the optimal estimation framework and it is the first guess of the state vector **X**,
323 $\mathbf{X_1}$ in Eq. (1). It provides a constraint on the ill-posed inversion problem. The prior is calculated
324 independently for each month of the year from climatological sounding profiles (using 10 years
325 of data) in the Denver area. **T**he covariance matrix, $\mathbf{S_a}$, of the "prior" vector includes not only
326 temperature or water vapor variances but also the covariances between them. Using around
327 3,000 radiosondes launched by the NWS in Denver, each radiosonde profile is interpolated to
328 the vertical levels used in the retrieval, after which the covariance of temperature and
329 temperature, temperature and humidity, and humidity and humidity is computed for different
330 levels. LWP is arbitrarily assigned in $\mathbf{X_a}$, with large values chosen for its uncertainty in $\mathbf{S_a}$, so that
331 it does not impact (constrain) the retrieval. Presently, the assumed uncertainty in LWP in the
332 prior is assigned to 200 g m^{-2} in TROPoe configuration file.
333 Four configurations are chosen for the observational vector **Y** ($\mathbf{Y_1}$, $\mathbf{Y_2}$, $\mathbf{Y_3}$, and $\mathbf{Y_4}$). In each
334 of these, the surface observations are obtained by the 2-m BAO *in-situ* measurements of
335 temperature and humidity. The MWR provides **Tb** measurements from 22 channels from the
336 zenith scan for the zenith only configuration ($\mathbf{Y_1}$), while when using the zenith plus oblique Tb
337 inputs ($\mathbf{Y_2}$, $\mathbf{Y_3}$, and $\mathbf{Y_4}$) the same 22 channels were used from the zenith scans together with only
338 the four opaque channels (56.66, 57.288, 57.964 and 58.8 GHz) from the oblique scans. Using

additional measurements from the co-located radar systems with RASS, the observational vector is further expanded with either RASS 915 ($\mathbf{Y_3}$) or RASS 449 ($\mathbf{Y_4}$) virtual temperature observations. The covariance matrix of the observed data, $\mathbf{S_\epsilon}$, depends on the chosen $\mathbf{Y_i}$ as seen in the matrix $\mathbf{S_{\epsilon i}}$ (with i = 1:4) descriptions, with increasing dimensions from $\mathbf{Y_1}$ to $\mathbf{Y_2}$ and additional increasing dimensions to $\mathbf{Y_3}$ or $\mathbf{Y_4}$ through the multi-level measurements of the RASS (Turner and Blumberg, 2019). Table 1 summarizes the observational information included in these four different configurations of the PR.

	T_{sfc}	Q_{sfc}	Tb_{zenith}	$Tb_{oblique}$	$Tv_{RASS915}$	$Tv_{RASS449}$
$\mathbf{Y_1}$ = *MWRz*	*X*	*X*	*X*			
$\mathbf{Y_2}$ = *MWRzo*	*X*	*X*	*X*	*X*		
$\mathbf{Y_3}$ = *MWRzo915*	*X*	*X*	*X*	*X*	*X*	
$\mathbf{Y_4}$ = *MWRzo449*	*X*	*X*	*X*	*X*		*X*

Table 1. Four PR configurations corresponding to the four observational $\mathbf{Y_i}$ vectors in Eq. (1).

The uncertainty in the MWR Tb observations was set to the standard deviation from a detrended time-series analysis for each channel during cloud-free periods. The method to detect those cloud-free periods is described in detail in Section 3.2. The derived uncertainties ranged from 0.3 K to 0.4 K in the 22 to 30 GHz channels, and 0.4 to 0.8 K in the 52 to 60 GHz

353 channels. We assumed that there was no correlated error between the different MWR
354 channels.

355 For the RASS, co-located RASS and radiosonde profiles were compared and the standard
356 deviation of the differences in Tv were determined as a function of the radar's signal-to-noise
357 ratio (SNR). This relationship resulted in uncertainties that ranged from 0.8 K at high SNR values
358 to 1.5 K at low SNR values. Again, we assumed that there was no correlated error between
359 different RASS heights. Following these assumptions, the covariance matrix $\mathbf{S_\varepsilon}$ is diagonal.

360 The Jacobian matrix, **K**, is computed using finite differences by perturbing the elements
361 of **X** and rerunning the forward model. It has dimensions m x 111, where m is the length of the
362 vector $\mathbf{Y_i}$, therefore its dimension increases correspondingly with the inclusion of more
363 observational data. **K** makes the "connection" between the state vector and the observational
364 data and should be calculated at every iteration.

365

366 **3.2 Bias-correction of MWR observations using radiosondes or climatology**

367 Observational errors propagate through retrieval into the derived profiles (i.e. the bias
368 of the observed data will contribute to a bias in the retrievals). For that, retrieval uncertainties
369 in Eq. (1) from $\mathbf{Y} = \mathbf{Y_1}$ or $\mathbf{Y_2}$ derive only from uncertainties in surface and MWR data, while
370 retrieval uncertainties from $\mathbf{Y} = \mathbf{Y_3}$ or $\mathbf{Y_4}$ come from uncertainties in the surface, MWR, and RASS
371 measurements.

372 The bias of the retrieval depends on both the absolute accuracy of the forward model
373 and on any observational systematic offset, of which the systematic error in the MWR
374 observations could potentially be reduced through application of an MWR Tb bias-correction

375 procedure. In this study, two different approaches were used for the bias-correction: the first is
376 based on a comparison to the radiosondes, while the second uses climatological profiles. The
377 first method could be used for a field campaign where occasional co-located radiosonde
378 launches are taken, while the second would be used for deployments without any supporting
379 radiosonde observations.

380 For both approaches, the first step is to identify clear-sky periods during which the bias
381 can be estimated (to eliminate uncertainties associated with clouds) and subsequently the bias
382 can be removed from the observed MWR Tbs. One method to identify clear-sky times is to use
383 a time-series of Tb observations in the 30 GHz liquid water sensitive channel of the MWR.

384 The standard deviation of the MWR Tb in the 30 GHz channel is calculated over a time
385 frame of one hour centered at the radiosonde launch time. The data from the zenith scan and
386 the averaged oblique scans are reviewed separately. Liquid-cloud free periods were identified
387 by cases where the temporal standard deviation was small (< 0.4 K), and more than 35
388 radiosonde profiles were classified as being launched in clear skies. The usage of the standard
389 deviation from the time-series from the oblique scans, with the same 0.4 K restriction, reduces
390 the number of the clear-sky radiosonde profiles to 18. For those chosen 18 radiosonde profiles,
391 the Tb is calculated from radiosonde temperature profiles through MonoRTM at each of the
392 MWR channels. The mean difference between these calculated radiosonde Tbs and measured
393 MWR Tbs forms the Tb bias with which the MWR Tb data can be corrected. This bias-correction
394 method will be referred to as 'radiosonde BC'.

395 While this radiosonde BC method can be employed for the XPIA dataset, for other
396 campaigns this approach would not be possible if co-located radiosonde observations were not

397 available. For this situation, an alternative method for correcting the MWR Tb biases is
398 presented. There are often spectral features in the observed minus computed brightness
399 temperature residuals that could not be explained by any physically realistic atmospheric
400 profiles, and can only result because of a calibration error in the observations. This alternative
401 bias-correction method is aimed purely to remove this unphysical spectral signature. In this
402 method, to choose clear-sky periods, the 30 GHz channel MWR Tb data are used on a daily
403 basis. The standard deviation of the MWR Tb is calculated as the average of standard deviations
404 in a one-hour sliding window through all data points of a day. Four clear-sky days were
405 identified using a threshold of 0.4 K on the standard deviation: March 10 and 30, and April 13
406 and 29, 2015. The Tb bias is then computed for each of the 22 channels as the averaged
407 difference between the observed Tb from the MWR zenith observations and the forward model
408 calculated Tbs at zenith using the TROPoe-retrieved profiles ($\mathbf{Y_1}$) of those selected clear-sky
409 days. This method identified spectral calibration errors in the MWR observations that could not
410 be explained by physically realistic atmospheric profiles. This bias-correction technique, which
411 accounts for those unphysical spectral calibration features, will be referred to as 'TROPoe BC'.
412 Fig. 1 shows the Tb biases found for all 22 MWR channels from both bias-correction
413 approaches. The biases calculated with the radiosonde BC scheme are shown for all channels
414 used in our analysis: 22 channels of the zenith scan, in red, and four V-band opaque channels of
415 the oblique scans, in blue. The black and green triangles represent the biases calculated using
416 the TROPoe BC approach for zenith and for zenith+oblique scans, respectively. All biases are
417 presented with associated uncertainties (error bars representing the standard deviation over all

radiosondes for radiosonde BC, and mean observation Tb vector uncertainties for chosen four clear-sky days for TROPoe BC).

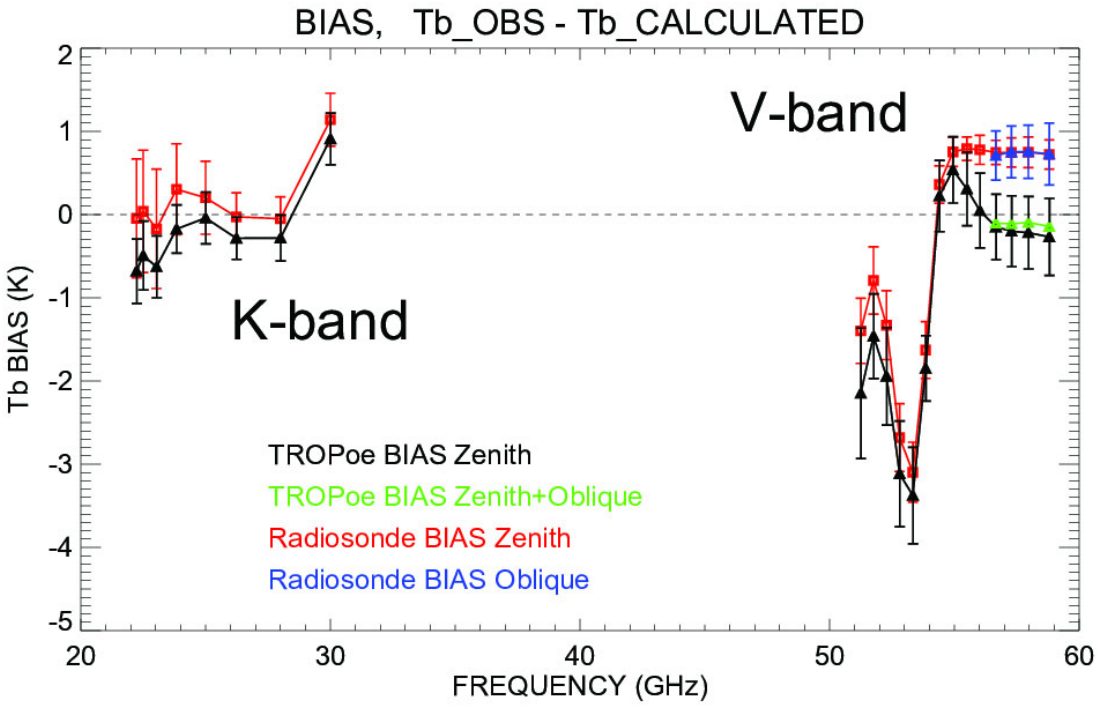

Fig. 1. Tb biases derived from the radiosonde BC method (and TROPoe BC method) in all 22 MWR channels of the zenith scan in red (and in black), and in the four opaque channels of the oblique scans in blue (and in green).

The biases from the two bias-correction schemes are within the uncertainties of each other for most of the channels except at the higher frequencies in the V-band. Biases in the most opaque channels are significantly affected by the accuracy of the boundary layer temperature profiles. When TROPoe BC is used, a monthly average prior temperature profile is used in the PR, and thus differences between this prior profile and the actual temperature

profile can result in a spectral bias in the more opaque MWR channels. On the contrary, the radiosonde BC uses a direct measurement of the temperature profile (from the radiosonde), and thus is more accurate. It is also important to note that, in both approaches, the biases in the opaque channels for zenith and for oblique scans (for radiosonde BC these are red and blue, respectively; and for the TROPoe BC these are black and green, respectively) are very similar to each other. This supports the assumption that the true bias is nearly independent of the scene, or that the sensitivity to the scene (e.g., zenith or off-zenith) is small.

The bias-correction methods were applied by removing the corresponding calculated biases from the MWR Tb observations before the retrievals were performed. Later in Section 4, differences in the retrieved temperature profiles will be shown when using the two bias-correction approaches. These differences will be more evident in the temperature profiles exhibiting near-ground temperature inversions.

However, the final goal of this study is not to assess the sensitivity to different bias-correction approaches but to verify that the inclusion of RASS observations does improve retrieved temperature profiles, independently of the bias-correction method used.

3.3 Analysis of physical retrieval characteristics

The retrieved profiles of the four different PR configurations presented in Table 1 (MWRz, MWRzo, MWRzo915, MWRzo449) were compared to the radiosonde profiles. To compare radiosonde observations against the PR profiles, all radiosonde profiles were interpolated vertically to the same PR heights, and PR profiles were averaged in the time window between 15 minutes before and 15 minutes after each radiosonde launch. Since the

451 radiosonde ascends quite quickly in the lowest kilometers of the atmosphere (~15-20 min to
452 reach 5 km), the 30-minute temporal window is estimated to be representative of the same
453 volume of the atmosphere measured by the radiosonde. BAO tower temperature and mixing
454 ratio data at the seven available levels were used as an additional validation dataset, without
455 any vertical interpolation, averaged in the time window between 15 minutes before and 15
456 minutes after each radiosonde launch.

457 As an example of the different temperature retrievals and their relative performance,
458 data obtained on 17 March 2015 at 2200 UTC are presented in Fig. 2. Temperature profiles up
459 to 2 km AGL retrieved from the four PR configurations (MWRz, MWRzo, MWRzo915,
460 MWRzo449, using the radiosonde BC) are compared to the radiosonde data in red and to the
461 BAO measurements in blue squares. Note that all four of the PRs match the BAO observations
462 reasonably well near the ground. The MWRz and MWRzo profiles are very smooth and depart
463 quite substantially from the radiosonde measurements, being unable to reproduce the more
464 detailed structure of the atmospheric temperature profile measured by the radiosonde, while
465 the MWRzo449 profile (in light-blue) demonstrates a better agreement with both the
466 radiosonde and BAO measurements (blue squares). The MWRzo915 profile (in purple) also tries
467 to follow the elevated temperature inversion observed by the radiosonde, successfully only in
468 the lower part of the atmosphere (below 1 km AGL) where RASS 915 measurements are
469 available. This behavior will be also addressed in the following section and in the statistical
470 analysis presented later in the manuscript.
471

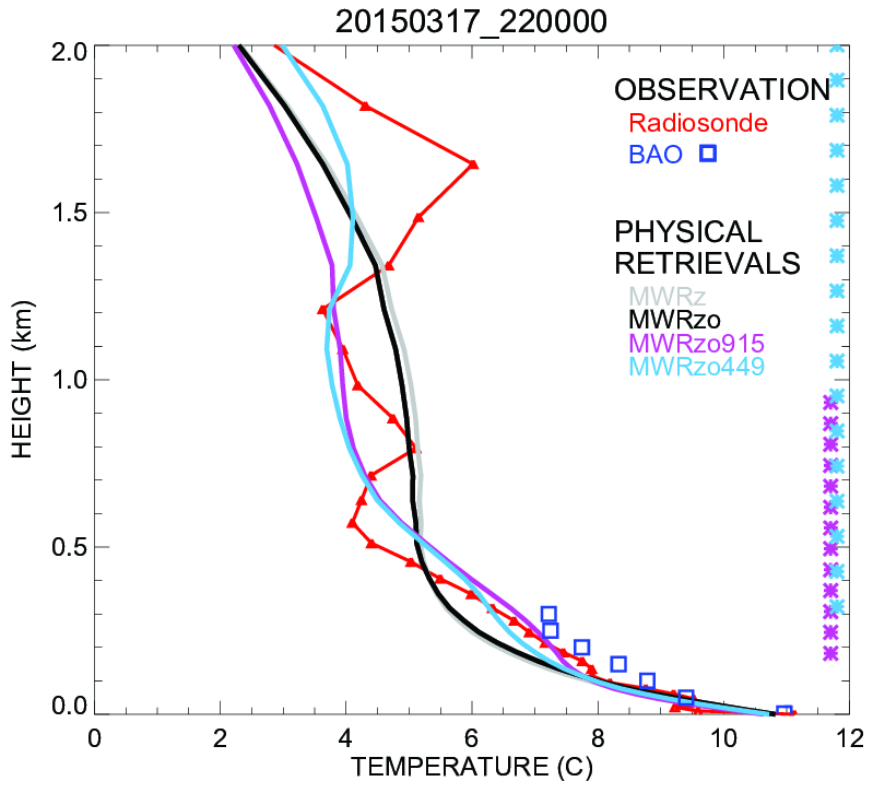

Fig. 2. Temperature profiles obtained by the four PR configurations, after applying the radiosonde BC on the MWR Tbs: MWRz in gray, MWRzo in black, MWRzo915 in purple, and MWRzo449 in light-blue. These retrievals are compared to radiosonde measurements, in red, and BAO tower observations, in blue squares. The heights with available RASS virtual temperature measurements (RASS 915 in purple and RASS 449 in light-blue) are marked by the asterisks on the right Y-axis.

An asset of TROPoe is that several characteristics of the PRs can be obtained from two matrices, the averaging kernel, **Akernel,** and the posterior covariance matrix, **Sop** (Masiello et al., 2012; Turner and Löhnert, 2014, Turner and Bloomberg, 2019), calculated as:

$$\boldsymbol{Akernel = B^{-1}\, K^{T}\, S_{\varepsilon}^{-1}\, K} \quad (2)$$

and:

$$\boldsymbol{Sop = B^{-1}} \quad (3)$$

where:

$$\boldsymbol{B = S_a^{-1} + K^{T}\, S_{\varepsilon}^{-1}\, K}$$

All matrices, **Akernel**, **Sop**, and **B**, have dimensions 111 x 111 in our configuration. While the top left corner of the **Akernel** matrix (1:55, 1:55) is devoted to temperature, called further in the text **ATkernel**, the next (56:110, 56:110) elements are devoted to the water vapor mixing ratio, called **AQkernel**.

The **Akernel** provides useful information about the calculated retrievals, such as vertical resolution and degrees of freedom for signal at each level. The rows of the **Akernel** provide the smoothing functions (Rodgers, 2000) that could be applied to the radiosonde profiles (Eq. 4) to minimize the vertical representativeness error in the comparison between the various retrievals and the radiosonde profiles due to very different vertical resolutions of these profiles (Turner and Löhnert, 2014).

Smoothed radiosonde observed profiles can be computed using the averaging kernel, as:

$$\boldsymbol{X_{smoothed\_radiosonde} = Akernel\ (X_{radiosonde} - X_a) + X_a} \quad (4)$$

The **Akernel** in Eq. (2) depends on the retrieval parameters (e.g., which datasets are used in the **Y** vector, the values assumed in the observation covariance matrix $\mathbf{S_\varepsilon}$, and the

505 sensitivity of the forward model), so for our four PR configurations it is possible to calculate
506 four different kernels from Eq. (2).

507 For each of the four **Akernel**s, a smoothed radiosonde profile can be computed for each
508 radiosonde profile using Eq. (4). In the presence of temperature inversions or other particular
509 structures in the atmosphere, these smoothed profiles can be quite different from each other
510 and also from the original unsmoothed radiosonde profile. Consequently, while comparison of
511 the retrievals to the relative Akernel-smoothed radiosonde profiles can be used to minimize the
512 vertical representativeness effects due to the different vertical resolutions of these profiles, we
513 note that a statistical comparison between the four configurations of the observational vector
514 would not be fair if each of their retrieved profiles is compared to a different Akernel-smoothed
515 radiosonde profile. Therefore, in the statistical analysis presented later in the manuscript
516 (section 4.2), mean bias, root mean square error (RMSE), and Pearson correlation coefficients
517 will be computed between the various TROPoe retrieval configurations and the unsmoothed
518 radiosonde profiles, just interpolated to the same vertical levels of the retrieved profiles.

519 The **ATkernel** can help understand the differences in the retrieved temperature profiles
520 obtained by the configurations using additional RASS data, shown in the example of Fig. 2.
521 Figure 3a includes the temperature profiles of the radiosonde (unsmoothed and **ATkernel**'s
522 smoothed) and PRs of MWRzo and MWRzo449 for the same example as in Fig. 2. Due to the
523 inclusion of RASS measurements, the **ATkernel**-smoothed radiosonde profile of the MWRzo449
524 configuration (dashed light-blue line) is closer to the original radiosonde data (in red) compared
525 to the black dashed profile of the MWRzo's **ATkernel**-smoothed radiosonde profile.
526 Additionally, the rows of the **ATkernel** provide a measure of the retrieval smoothing as a

527 function of altitude, so the full-width half maximum (FWHM) of each **ATkernel** row estimates
528 the vertical resolution of the retrieved solution at each vertical level (Maddy and Barnet, 2008;
529 Merrelli and Turner, 2012). Plots of this vertical resolution as a function of the height for the
530 MWRzo PR and for the MWRzo449 PR are included in Fig. 3b. This plot shows that the
531 additional observations from the RASS 449 significantly improve the vertical resolution of the
532 retrievals.

533 The posterior covariance matrix, **Sop,** provides a measure of the uncertainty of the
534 retrievals while the square root of the diagonal of this matrix is used to specify the 1-σ errors in
535 the profiles of temperature or mixing ratio. Also, **Sop** shows the level-to-level dependency of
536 the retrievals, and in an ideal case should have all non-diagonal elements equal to zero.
537 Converted to a correlation matrix, it is possible to visualize these dependencies, as presented in
538 Fig. 3c, d. The use of additional RASS data (MWRzo449 **Sop**, Fig. 3d) reduces the off-diagonal
539 covariances, therefore substantially decreasing the correlations in those areas compared to the
540 MWRzo **Sop** (Fig. 3c).

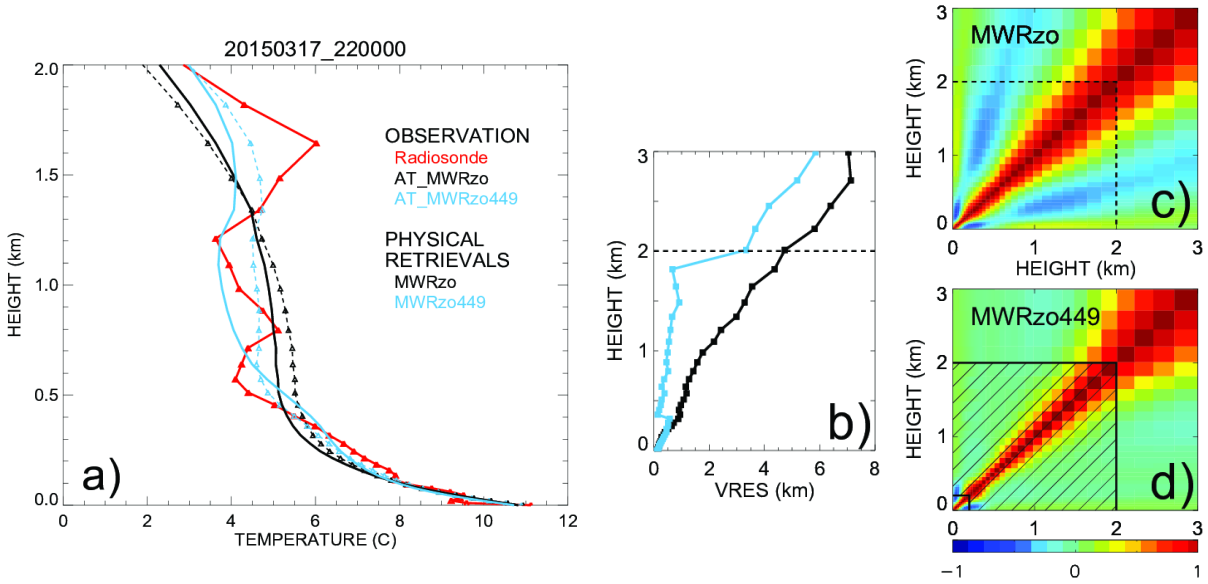

541

*Fig. 3. a) observed temperature profiles from radiosonde, in red, from **ATkernel**s smoothed radiosonde, **AT_MWRzo** in dashed black, and **AT_MWRzo449** in dashed light-blue; PRs from MWRzo PR in solid black, and from MWRzo449 PR in solid light-blue. b) vertical resolution (VRES) as a function of the height for the MWRzo PR (black), and for the MWRzo449 PR (light-blue). c) and d) 3 x 3 km (37 x 37 levels) **Sop** matrices, converted to correlation matrices, for the MWRzo PR (c), and for the MWRzo449 PR (d). Dashed lines on plots b)-d) mark 2 km AGL. Hatched area on panel d marks the RASS measurement heights.*

To understand the level-to-level correlations among the 4 different retrieval configurations in Table 1, the **Sop** matrices were averaged over all radiosonde events, and converted to correlation matrices (Fig. 4). A clearly visible narrowing of the spread around the main diagonal and correlation reduction in the off-diagonal elements result by adding additional observations, from MWR zenith only (Fig. 4a), to MWR zenith-oblique (Fig. 4b), to the larger impact obtained by the usage of the RASS 915 (Fig. 4c), concluding with the RASS 449 (Fig. 4d) data. The mean retrieval uncertainty profile for each of the PR configurations is presented in Fig. 4e. The uncertainty of the MWRzo449 retrieval up to 1 km AGL is around 0.5 ^{o}C while the other retrievals have higher uncertainties of up to 1 ^{o}C. The higher accuracy of the MWRzo449 retrievals is because that configuration has more observational information compared to the other retrieval configurations.

Other statistically important features to analyze in the PRs, besides their uncertainty, are the vertical resolution already introduced in the example of Fig. 3b, and the degree of freedom for signal (DFS). These two features, derived from the **Akernel**s of each PR

564 configuration, averaged over all radiosonde events, are shown in Fig 4f and 4g. The vertical
565 resolution (Fig. 4f) shows the width of the atmosphere layer used for each retrieval height,
566 computed as the full-width half-maximum value of the averaging kernel. The cumulative DFS
567 profile (Fig. 4g) is a measure of the number of independent pieces of information in the
568 observations below the specified height. For example, at the 1 km AGL level the vertical
569 resolution of MWRzo449 is 0.5 km (i.e. information is from +/- 0.5 km around the retrieval
570 height is considered in the retrieval), while all other retrievals use the information from more
571 than +/- 1.5 km. Also, the DFS, as a cumulative measure, shows an increase in pieces of
572 information from MWRz to MWRzo for the whole profile and from MWRzo to MWRzo915 and
573 to MWRzo449 above ~0.2 km where RASS data are available. The DFS of MWRzo915 is higher
574 compared to the DFS of MWRzo449 in the 0.2-0.5 km AGL layer because RASS 915 data have
575 denser measurements there. It is also important to note that there is no additional information
576 added to any of the retrievals above 2km AGL, i.e. the slope of the cumulative DFS profiles are
577 equal. Despite that, the statistical analysis of the PRs up to 3 km AGL, shown in Section 4, will
578 prove that the retrieval improvements obtained by including the RASS are found even above
579 the height of the RASS measurements availability.
580

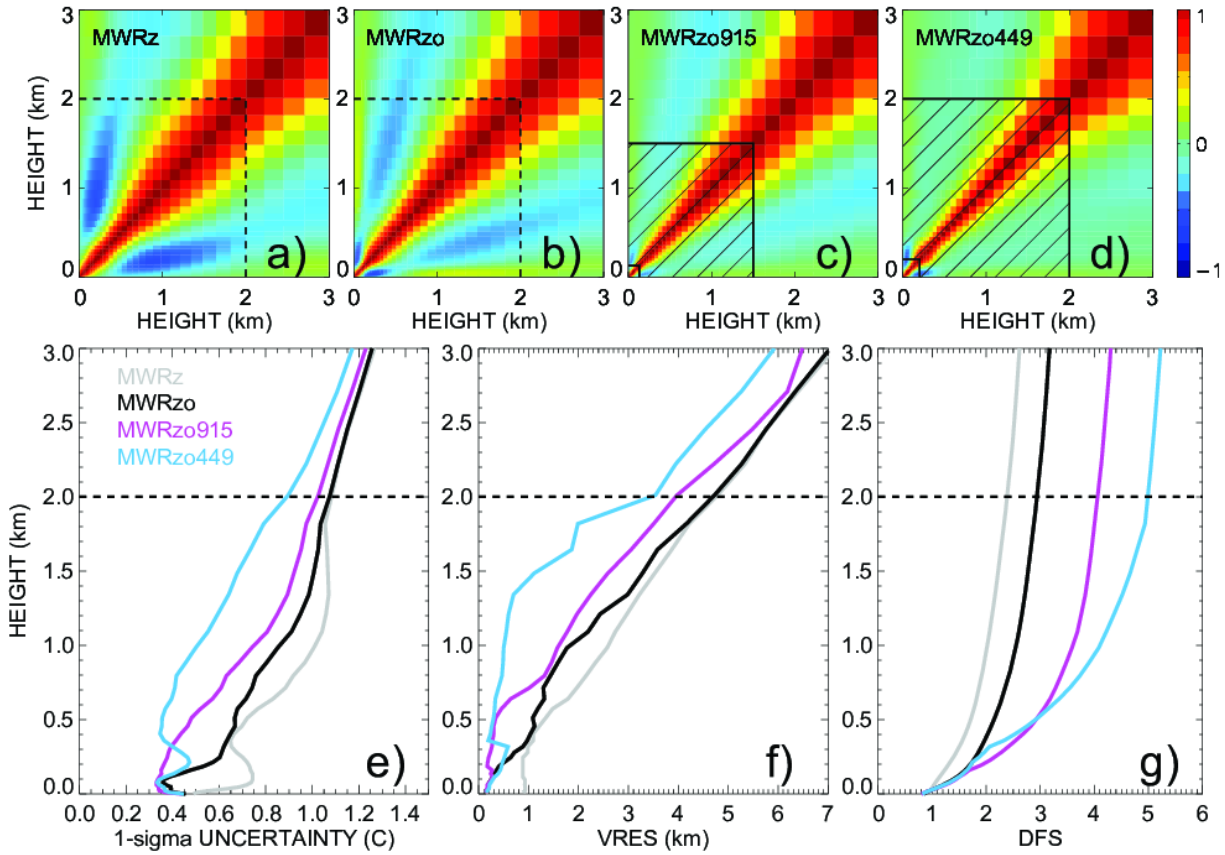

581

582 *Fig. 4. Top row: The mean **Sop**s, displayed as correlation matrices, for (a) MWRz, (b) MWRzo, (c)*

583 *MWRzo915, and (d) MWRzo449, averaged over all radiosonde events. Hatched area on panels*

584 *c) and d) marks the RASS maximum measurement heights. Bottom panels: (e) one-sigma*

585 *uncertainty derived from the posterior covariance matrix in ^{o}C, (f) vertical resolution (VRES) in*

586 *km, and (g) cumulative Degree of Freedom (DFS) as a function of height for temperature,*

587 *averaged over all radiosonde events (MWRz is in gray, MWRzo is in black, MWRzo915 is in*

588 *purple, and MWRzo449 is in light-blue). Dashed lines mark 2 km AGL on all panels.*

589

590 The improvements from MWRz (in gray) to MWRzo (in black), to MWRzo915 (in purple),

591 and finally to MWRzo449 (in light-blue) are visible in all three panels (Fig 4e-g), whereas

MWRzo449 has the lowest 1-σ uncertainty and highest DFS compared to the other PRs, particularly below 2 km AGL, where RASS 449 measurements are available. Finally, it is interesting that below 200 m AGL the MWRzo915 has slightly smaller lowest 1-σ uncertainty and vertical resolution relative to the MWRzo449, as could be expected due to the first available height of the RASS 915 being lower (120 m AGL) than the first available height for the RASS 449 (217 m AGL) and due to the finer vertical resolution of the 915-MHz RASS. This suggests that if additional observations were available in the lowest several 100 m of the atmosphere where RASS measurements are not available, improvements might be even better closer to the surface, where temperature inversions, if present, are sometimes difficult to retrieve correctly.

4. Results

4.1 Statistical analysis of physical retrievals up to 3km AGL

Several cases were found during XPIA when the temperature profile exhibited inversions, with the lowest happening in the surface layer. Figure 5 shows one of the most complex cases, with several temperature inversions visible in the temperature profile from the radiosonde (red line), in the temperature measurements from the BAO tower (blue squares), and in the virtual temperature measured by the RASS 449 (light blue triangles). Note that the virtual temperature profile is in close agreement with the temperature measured by radiosonde.

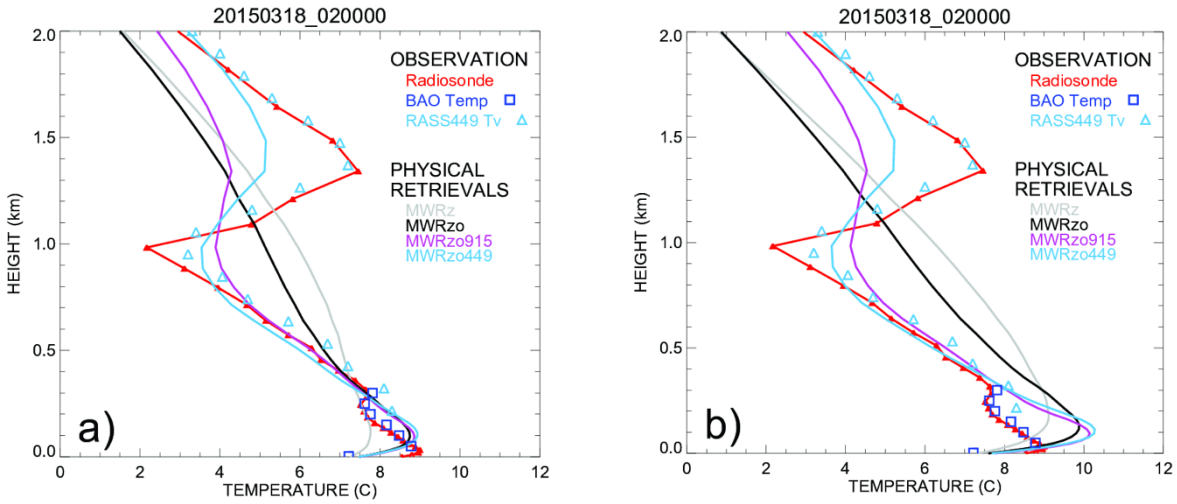

612

613 *Fig. 5. As in Fig. 2 but for 18 March 2015 at 0200 UTC. The RASS 449 virtual temperature is*
614 *included as light blue triangles. a) shows the PRs obtained after applying the radiosonde BC, and*
615 *b) shows the PRs obtained after applying the TROPoe BC on the MWR Tbs.*

616

617 Figure 5 also illustrates the difference in the temperature profiles, especially between 0-
618 300m AGL, for the two different bias-correction schemes, which show noticeable differences in
619 the biases of the opaque channels (especially important for the near-ground retrievals)
620 presented in Fig. 1. As expected, the radiosonde BC method yielded a retrieved profile closer to
621 the radiosonde temperature profile than when using TROPoe BC, for which the inversion in the
622 temperature profile close to the surface is too accentuated (particularly the black, purple, and
623 cyan lines, all of which used oblique scan data).

624 The relative statistical behavior (Pearson correlation, RMSE, and bias) of the PRs for
625 both temperature and mixing ratio against radiosondes is shown in Figure 6, using both bias-
626 correction approaches. PRs obtained after applying the radiosonde BC (Fig. 6a) present overall

627 smaller RMSE and bias (the latter almost equal to zero up to 3 km AGL) and slightly higher
628 correlations compared to the statistics of the PRs obtained after applying the TROPoe BC (Fig.
629 6b). This could be expected since for the comparison in Fig. 6a a subset of the radiosondes was
630 already used for the Tb bias correction. Also, the different retrievals show a narrower
631 distribution for the panels in Fig. 6a. Nevertheless, the results obtained when applying either
632 bias-correction methods (in Fig. 6a, b) consistently show the improvement obtained when the
633 RASS observations are used, with relatively smaller bias and RMSE in the 3 km layer AGL. The
634 correlation is mainly improved above 1 km, when RASS observations are included.

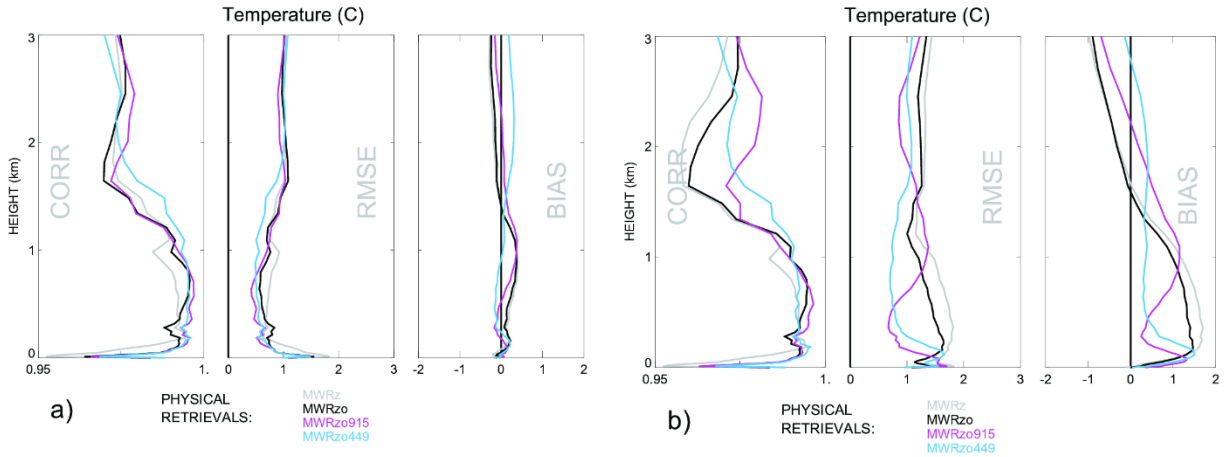

635 *Fig. 6. Pearson correlation, RMSE, and mean bias for temperature profiles of MWRz in gray,*
636 *MWRzo in black, MWRzo915 in purple, and MWRzo449 in light-blue for the radiosonde BC bias-*
637 *correction method in a) and TROPoe BC method in b).*

638

639 Besides temperature profiles, the PRs also provide water vapor mixing ratio profiles. It is
640 understandable that the different configurations of PRs are not noticeably different from each
641 other in relation to moisture, because the Tv observations from the RASS are dominated by the
642 ambient temperature (not moisture), and thus have little impact on the water vapor retrievals.

643 We found that the **AQKernel**s are almost identical for all four PR configurations (not shown).
644 Detailed statistical evaluation of the PRs mixing ratio profiles are presented in Fig, 7, also
645 averaged over all radiosonde events, and show very similar correlations, RMSEs, and biases for
646 all PRs, implying that the impact of including RASS observations in the retrieval is minimal on
647 this variable. Finally, it is noted that Fig. 7 shows the mixing ratio of the data from TROPoe BC.
648 The radiosonde BC mixing ratio results are almost identical.

650
651
652
653
654
655

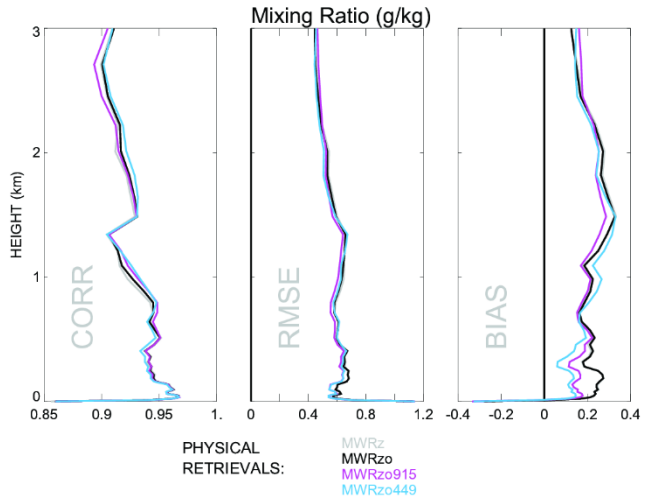

656 *Fig. 7. Same as the panels in Fig. 6b, but for mixing ratio, when using the TROPoe BC method on*
657 *the MWR Tbs.*
658

659 **4.2 Statistics for the profiles least close to the climatology**

660 Physical retrievals use climatological data as a constraint in the retrieval. Statistically,
661 the averaged profiles of both temperature and moisture variables are very close to the
662 climatological averages. However, the most interesting and difficult profiles to retrieve are the
663 cases furthest from climatology (Löhnert and Maier, 2012). To check the behavior of the
664 retrieved data in such "extreme" cases, the RMSE was first calculated for each radiosonde

665 profile relative to the prior profiles for 37 vertical levels from the surface up to 3 km AGL, and
666 then the 15 cases with the largest 0-3 km layer averaged RMSEs compared to the prior were
667 selected.

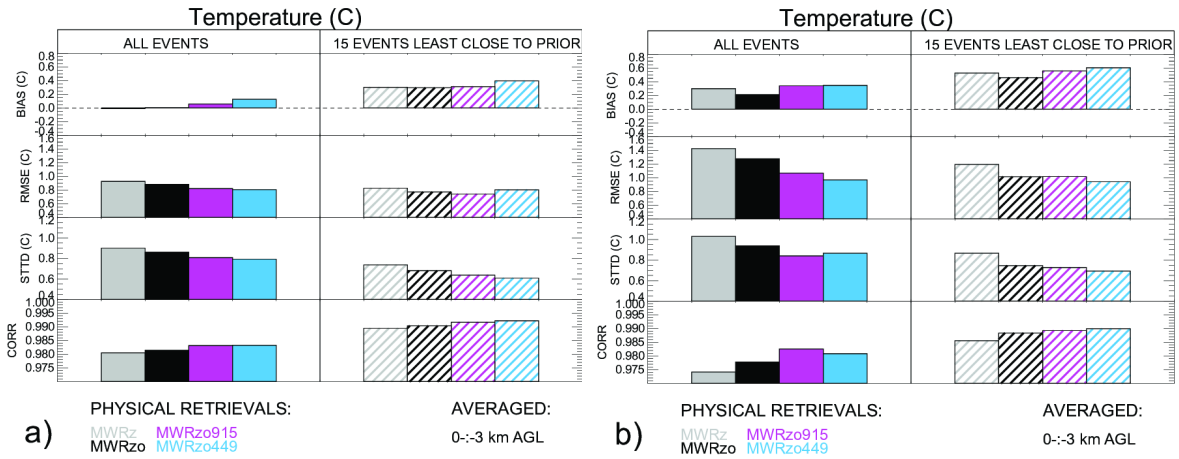

668 *Fig. 8. From top to bottom: biases (retrievals minus radiosonde), RMSEs, standard deviations of*
669 *the difference between retrievals and radiosonde, and Pearson correlations for the four PR*
670 *configurations, averaged from the surface to 3 km AGL, and over all radiosonde data (solid*
671 *boxes), and over the 15 extreme cases (hatched boxes). The data in panels a) use radiosonde BC,*
672 *and in b) TROPoe BC on the MWR Tbs.*

673 Figure 8 shows the temperature statistical analysis for the entire radiosonde data set
674 (solid boxes) and for the fifteen events far from the climatological mean (hatched boxes) for
675 bias, RMSE, standard deviation of the differences between retrievals and radiosonde data, and
676 Pearson correlation, calculated as the weighted averaged over the 37 vertical heights up to 3
677 km AGL[1].

[1] The vertical grid used in the PRs is not uniform, with more frequent levels closer to the surface. If a simple average of the data from all levels is used, the near-surface layer will be weighted more compared to the upper levels of the retrievals. To avoid this, a vertical average over the lowest 3 km AGL is performed using weights at each vertical level determined by the distance between the levels.

678 Differences in the statistics when using the entire radiosonde data set or the fifteen
679 extreme profiles are noticeable for all statistical estimators. The PRs that include RASS
680 observations show better performance compared to the strictly MWR-only PR profiles (i.e.,
681 MWRz and MWRzo) for almost all statistical comparisons. This improvement is larger for the
682 PRs using the TROPoe BC (Fig. 8b) compared to the PRs using the radiosonde BC (Fig. 8a). Three
683 statistical estimators, RMSE, standard deviation, and Pearson correlation show overall better
684 values for the 15 extreme cases compared to the whole radiosonde dataset, for all PR
685 configurations and both BC approaches. This is due to the fact that for this dataset the monthly
686 averaged radiosonde profiles (for March and May particularly) depart quite substantially from
687 the monthly prior profiles. For example, the averaged radiosonde profile in March is warmer by
688 ~7 ^{o}C compared to the March prior (and in May by ~5 ^{o}C) in the first 3 km AGL. Consequently,
689 the extreme cases (mostly found in March) have the warmest radiosonde temperature profiles,
690 but are overall closer to the monthly averaged radiosonde profiles.
691 Table 2 includes the same data as in Figure 8 but as a percentage of the improvement,
692 compared to the MWRz retrievals.
693
694
695
696
697
698

0-3 km AGL	ALL EVENTS					15 EVENTS LEAST CLOSE TO THE PRIOR			
RADIOSONDE BIAS-CORRECTION									
	MWRz	MWRzo	MWRzo RASS915	MWRzo RASS449		MWRz	MWRzo	MWRzo RASS915	MWRzo RASS449
RMSE	0%	5%	11%	13%		0%	7%	10%	3%
STTD	0%	4%	10%	12%		0%	8%	14%	17%
CORR	0%	0.1%	0.3%	0.3%		0%	0.1%	0.2%	0.3%
TROPoe BIAS-CORRECTION									
RMSE	0%	10%	25%	32%		0%	15%	15%	21%
STTD	0%	9%	18%	16%		0%	14%	16%	20%
CORR	0%	0.4%	0.9%	0.7%		0%	0.3%	0.4%	0.4%

699

700 *Table 2. Retrieval improvements for different RASS/MWR configurations as a percentage*

701 *compared to MWRz.*

702

703 The results presented in Table 2 show improvements in all statistical estimations when

704 including RASS observations, with improvements in RMSE between 10 and 20 %, demonstrating

705 the positive impact derived by the inclusion of the active measurements, regardless of the bias-

706 correction method used, but larger for the TROPoe BC data because there is more room for

707 improvement when this BC method is used. Improvements in the Pearson correlation

coefficients are small because correlation, determined during XPIA by the overall temperature structure with height and diurnal cycle, is already good, leaving little room for improvement.

4.3 Virtual temperature profile statistics

Using the physical retrieval outputs, “retrieved virtual temperature profiles” can also be calculated. In this section the direct comparison of these retrieved virtual temperature profiles and RASS virtual temperature profiles to the original radiosonde is shown. With this comparison we want to show how the biases of the retrieved profiles relate to the original RASS Tv biases.

Figure 9 shows Tv retrieved profile biases compared to the original radiosonde data. These Tv profiles and RASS 915 and RASS 449 Tv bias data are interpolated onto a regular vertical grid, going from 200 m to 1.6 km with a 100 m resolution, for easy comparison.

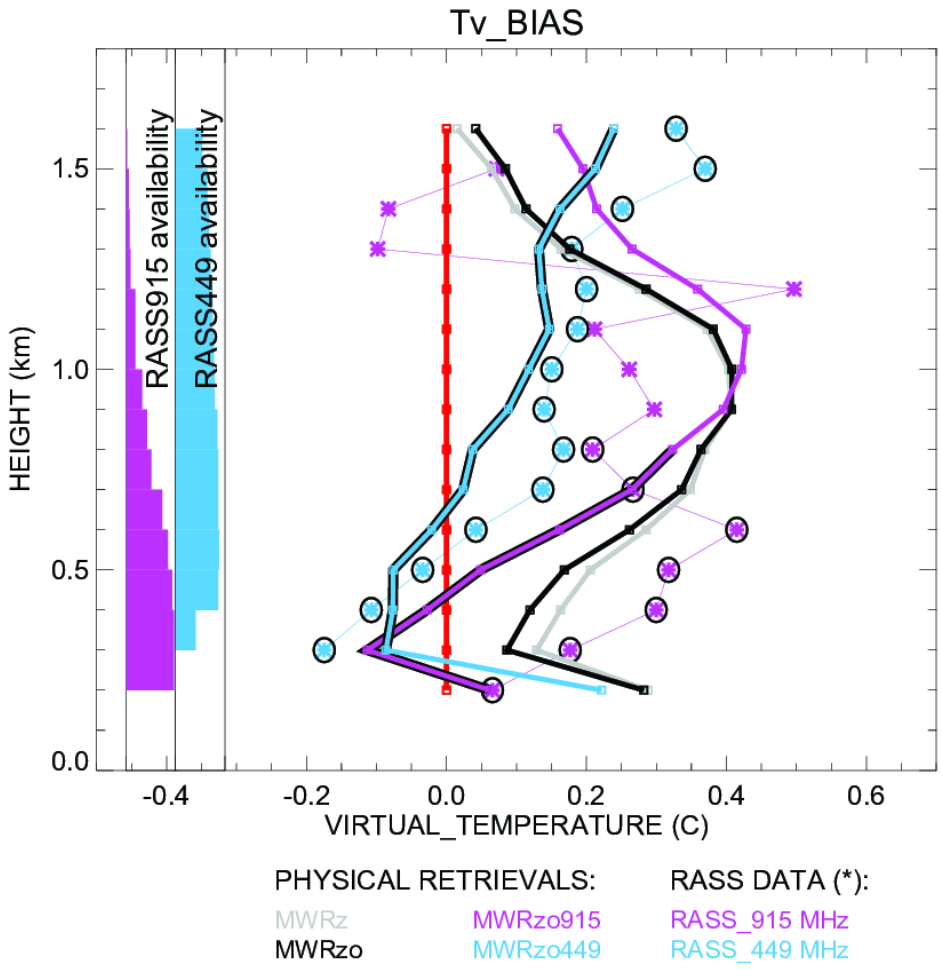

719

720 *Fig. 9. Bias of virtual temperature for all PR configurations compared to the original radiosonde*

721 *measurements. A zero bias is denoted by the red line. RASS data biases are marked by asterisks*

722 *and by additional circles for the RASS data with more than 50% availability, according to the*

723 *availability bar charts on the left.*

724 *All PRs profiles are derived after applying the radiosonde BC method.*

725

726 While RASS 449 data are available at almost all heights up to 1.6 km, the RASS 915 data

727 availability decreases considerably with height, lowering to 50% availability around 800 m AGL.

728 The PRs that include RASS data, MWRzo915 and MWRzo449, are also marked with additional
729 black lines at the heights with at least 50% of relative RASS data availability. In agreement with
730 Fig. 6a, this figure clearly shows the superiority of the MWRzo449 and MWRzo915 (in the layer
731 with > 50% RASS data availability) compared to the MWRz and MWRzo configurations, which
732 do not include RASS data. For MWRzo449, RASS 449 data were almost always available,
733 therefore it is easy to identify a similarity between the Tv bias profiles of the RASS 449 and the
734 PRs including it. Thus, for the MWRzo449 the Tv bias is more uniform through the heights
735 compared to all other PRs that do not include RASS data. Moreover, it is noted a roughly
736 constant offset between the MWRzo449 Tv and RASS 449 Tv biases profiles, with their
737 averaged difference equal to ~0.08 ^{o}C (when the radiosonde BC is used), and to ~0.32 ^{o}C (when
738 the TROPoe BC is used, not shown), over the ~1.3 km (0.3-1.6 km) atmospheric layer where
739 more than 50% of the RASS 449 measurements are available, uniformly distributed through the
740 heights. The inclusion of the RASS into the PRs does reduce the values of the biases in the
741 retrievals even below the values of the RASS biases, because of the combined information from
742 RASS and MWR.
743

744 **5. Conclusions**

745 In this study, data collected during the XPIA field campaign were used to test different
746 configurations of a physical-iterative retrieval (PR) approach in the determination of
747 temperature and humidity profiles from data collected by microwave radiometers, surface
748 sensors, and RASS measurements. The accuracy of several PR configurations was tested: two
749 configurations made use only of surface observations and MWR observed brightness

750 temperature (zenith only, MWRz; and zenith plus oblique, MWRzo); while two others included
751 the active virtual temperature profile observations available from co-located RASS (one, RASS
752 915, associated with a 915-MHz; and the other, RASS 449, associated with a 449-MHz wind
753 profiling radar). Radiosonde launches were used for verification of the retrieved profiles. In
754 Appendix A, the performance of MWRz and MWRzo retrieved profiles and Neural Network
755 retrieved profiles against the radiosondes was evaluated.

756 To remove any observational systematic error in the MWR Tb observations, two bias-
757 correction procedures were tested. The first one takes advantage of the many radiosondes
758 launched during XPIA, and the second one uses climatological profiles. As expected, the
759 radiosonde bias-correction method gives retrieved profiles closer to the radiosonde
760 temperature profiles than when using the climatological based method. Nevertheless, our
761 results show that regardless of the bias-correction method used, the inclusion of the
762 observations from the active RASS instruments in the PR approach improves the accuracy of the
763 temperature profiles by around 10-20% compared to the PR configuration using only surface
764 observations and MWR observed brightness temperature from the zenith scan. Of the PRs
765 configurations tested, generally better statistical agreement is found with the radiosonde
766 observations when the RASS 449 is used together with the surface observations and brightness
767 temperature from the zenith and averaged oblique MWR observations.

768 The **AKernel** and the posterior covariance matrices for temperature are used to derive
769 the one-sigma uncertainty, vertical resolution, and cumulative degree of freedom as a function
770 of height for the different PRs, and the level-to-level correlated uncertainty of the retrievals.
771 Results show that the inclusion of the active instruments improves all of the above-mentioned

772 variables in the 0-3km layer, including at heights between 2-3km that are above the maximum
773 RASS height. Thus, the positive impact of the RASS observations extends into the atmosphere
774 above the height of measurements themselves.

775 Furthermore, 15 cases when temperature profiles from the radiosonde observations
776 were the furthest away from the mean climatological average were selected, and the statistical
777 comparison was reproduced over this subset of cases. These are the cases usually the most
778 difficult to retrieve and the most important to forecast; therefore, it is essential to improve the
779 retrievals in these situations. Even for this subset of selected cases the inclusion of active
780 sensor observations in the PRs is found to be beneficial.

781 Finally, the impact of the inclusion of RASS measurements on the retrieved humidity
782 profiles was considered, but the inclusion of RASS observations did not produce significantly
783 better results, compared to the configurations that do not include them. This was not a surprise
784 as RASS measures virtual temperature, effectively adding very little extra information to the
785 water vapor retrieval. In this case a better option would be to consider adding other active
786 remote sensors such as water vapor differential absorption lidars (DIALs) to the PRs. Turner and
787 Löhnert (2021) showed that including the partial profile of water vapor observed by the DIAL
788 substantially increases the information content in the combined water vapor retrievals.
789 Consequently, to improve both temperature and humidity retrievals a synergy between MWR,
790 RASS, and DIAL systems would likely be necessary.

791

792 **Appendix A**

793 The neural network (NN) retrievals developed by the vendor explicitly for XPIA use a
794 training dataset based on a 5-year climatology of profiles from radiosondes launched at the
795 Denver International Airport, 35 miles south-east from the XPIA site. NN-based MWR vertical
796 retrieval profiles were obtained using the zenith or an average of two oblique elevation scans,
797 15- and 165-degrees (not including the zenith), all with 58 levels extending from the surface up
798 to 10 km, with nominal vertical grid depending on the height (every 50 m from the surface to
799 500 m, every 100 m from 500 m to 2 km, and every 250 m from 2 to 10 km, AGL).
800 Fig. 1A shows composite NN vertical profiles of temperature (separately for the zenith
801 and averaged obliques) calculated for radiosonde launch times, and the corresponding PR
802 profiles already introduced in Fig. 6a, b with additional TROPoe retrievals without any bias-
803 correction. For a proper comparison, only MWRz and MWRzo profiles are used, without
804 including RASS measurements. It has to be noted that since the “NN oblique” retrieval provided
805 by the manufacturer of the radiometer does not include the zenith, this configuration cannot
806 be considered exactly equivalent to the MWRzo PR.
807
808
809
810
811
812
813
814

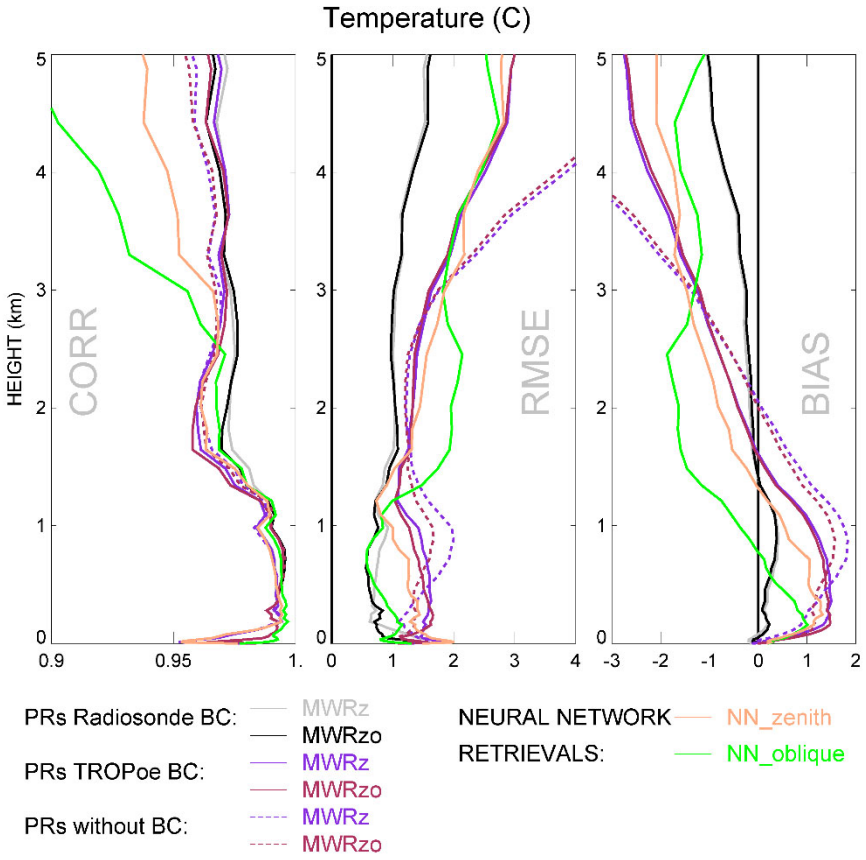

827 *Fig. 1A. Pearson correlation, RMSE, and mean bias for temperature profiles for MWRz in grey*
828 *(and purple) and MWRzo in black (and maroon) when the radiosonde BC (and the TROPoe BC)*
829 *method is applied. TROPoe temperature retrievals without any bias-correction are shown for*
830 *MWRz in dashed purple and for MWRzo in dashed maroon. Included in this figure are the NN*
831 *temperature profiles, from the zenith scan (in beige), and from the averaged oblique scans (in*
832 *green).*

833

834 Another difference to point out is that, while the MWR Tb data have been bias-
835 corrected before being used in the PR configurations, as discussed in Section 3.2, the NN
836 retrievals use the uncorrected Tb, since it was non-trivial to reprocess those retrievals. For

837 additional comparison we included TROPoe retrievals that use uncorrected Tbs. Martinet et al.
838 (2015) showed that when it is possible to bias-correct the MWR Tb before applying the NN
839 retrieval technique, the NN retrievals are not impacted below 1 km AGL, but a clear
840 improvement of NN retrievals in terms of RMSE and bias are observed between 1 and 3 km
841 altitude. As is visible in Fig. 1A, this is the layer of the atmosphere where the NN profiles (beige
842 and green lines) have larger bias and RMSE, compared to the PR profiles.

843 When the radiosonde BC method is used, the MWRz and MWRzo PRs (gray and black
844 lines) present better statistics through the entire profiles shown in Fig. 1A, with larger values of
845 the correlation coefficient, and smaller values of RMSE and bias. The oblique only NN profiles
846 (in green) show comparable statistics to the PRs employing the radiosonde BC method up to 1
847 km AGL, with degraded performances above this height. Above 1 km AGL, the zenith NN
848 profiles (in beige) do better than the oblique NN in terms of RMSE and bias. When the TROPoe
849 BC method is used, the MWRz and MWRzo PRs (purple and maroon lines) perform better than
850 the NN profiles only in terms of RMSE and bias, and only between 1.5 and 3 km AGL. The PRs
851 without any Tb bias-correction (dashed lines in Fig. 1A) clearly indicate that the BC is useful and
852 needed, showing very noticeable degradation in all three statistical measures above 3 km, and
853 larger RMSE and bias in 0.5-1.5 km AGL compared to TROPoe BC method.

854 The better performance obtained by the MWRz and MWRzo PRs that use the
855 radiosonde BC approach demonstrate the importance of having an accurate and reliable
856 method for bias correcting the MWR.

857

858 **Data availability**

All data are publicly accessible at the DOE Atmosphere to Electrons Data Archive and Portal, found at https://a2e.energy.gov/projects/xpia (Lundquist et al., 2016).

Author contribution

Irina Djalalova completed the primary analysis using the XPIA dataset. Daniel Gottas contributed to the post-processing of the RASS data. Dave Turner modified the TROPoe algorithm to include the RASS data as input. All authors contributed to the analysis of the results. Irina Djalalova prepared the manuscript with contributions from all co-authors.

Acknowledgements

We thank all the people involved in XPIA for instrument deployment and maintenance, data collection, and data quality control, and particularly the University of Colorado Boulder for making the CU MWR data available. We are very grateful for the constructive comments and suggestions provided by the two anonymous Referees and by the Editor, which we believe have greatly improved the clarity of the manuscript. Funding for this study was provided by the NOAA/ESRL Atmospheric Science for Renewable Energy (ASRE) program.

Competing interests

The authors declare no competing interests.

References

880 Adachi, A. and H. Hashiguchi: Application of parametric speakers to radio acoustic sounding
881 system. **ATMOS MEAS TECH**, **12**, 5699–5715, https://doi.org/10.5194/amt-12-5699-
882 2019, 2019.
883 Adler, B., J. M. Wilczak, L. Bianco, I. Djalalova, J. B. Duncan Jr., D. D. Turner: Observational case
884 study of a persistent cold air pool and gap flow in the Columbia River Basin. **J APPL**
885 **METEOROL CLIM**, 60, 1071-1090, https://doi.org/10.1175/JAMC-D-21-0013.1, 2021.
886 Banta, R. M., and coauthors: Characterizing NWP model errors using Doppler lidar
887 measurements of recurrent regional diurnal flows: Marine-air intrusions into the
888 Columbia River Basin. **MON WEATHER REV**, **148**, 927-953,
889 https://doi.org/10.1175/MWR-D-19-0188.1, 2020.
890 Bianco L., D. Cimini, F. S. Marzano, and R. Ware: Combining microwave radiometer and wind
891 profiler radar measurements for high-resolution atmospheric humidity profiling, **J**
892 **ATMOS OCEAN TECH**, **22**, 949–965, https://doi.org/10.1175/JTECH1771.1, 2005.
893 Bianco, L., K. Friedrich, J. M. Wilczak, D. Hazen, D. Wolfe, R. Delgado, S. Oncley, and J. K.
894 Lundquist: Assessing the accuracy of microwave radiometers and radio acoustic
895 sounding systems for wind energy applications. **ATMOS MEAS TECH**, **10**, 1707-1721,
896 https://doi.org/10.5194/amt-10-1707-2017, 2017.
897 Cadeddu, M. P., J. C. Liljegren, and D. D. Turner: The Atmospheric radiation measurement
898 (ARM) program network of microwave radiometers: instrumentation, data, and
899 retrievals, **ATMOS MEAS TECH**, **6**, 2359–2372, https://doi.org/10.5194/amt-6-2359-
900 2013, 2013.

901 Cimini, D., T. J. Hewison, L. Martin, J. Guldner, C. Gaffard, F. S. Marzano: Temperature and
902 humidity profile retrievals from ground-based microwave radiometers during TUC,
903 **METEOROL Z**, Vol. 15, No. 5, 45-56, DOI: 10.1127/09411-D-2948/2006/0099, 2006.
904 Cimini, D., E. Campos, R. Ware, S. Albers, G. Giuliani, J. Oreamuno, P. Joe, S. E. Koch, S. Cober,
905 and E. Westwater: Thermodynamic Atmospheric Profiling during the 2010 Winter
906 Olympics Using Ground-based Microwave Radiometry, **IEEE T GEOSCI REMOTE**, **49**, 12,
907 https://doi.org/10.1109/TGRS.2011.2154337, 2011.
908 Cimini, D., Rosenkranz, P. W., Tretyakov, M. Y., Koshelev, M. A., and Romano, F.: Uncertainty of
909 atmospheric microwave absorption model: impact on ground-based radiometer
910 simulations and retrievals, **ATMOS CHEM PHYS**, **18**, 15231–15259,
911 https://acp.copernicus.org/articles/18/15231/2018, 2018.
912 Cimini, D., M. Haeffelin, S. Kotthaus, U. Löhnert, P. Martinet, E. O'Connor, C. Walden, M.
913 Collaud Coen, and J. Preissler: Towards the profiling of the atmospheric boundary layer
914 at European scale—introducing the COST Action PROBE. **Bulletin of Atmospheric**
915 **Science and Technology**, **1**, 23–42, https://doi.org/10.1007/s42865-020-00003-8, 2020.
916 Clough, S.A., M. W. Shephard, E. J. Mlawer, J. S. Delamere, M. Iacono, K. E. Cady-Pereira, S.
917 Boukabara and P. D. Brown: Atmospheric radiative transfer modeling: A summary of the
918 AER codes, **J QUANT SPECTROSC RA**, vol 91, no. 2, pp 233-244,
919 https://doi.org/10.1016/j.jqsrt.2004.05.058, 2005.
920 Crewell, S., U. Löhnert: Accuracy of Boundary Layer Temperature Profiles Retrieved With
921 Multifrequency Multiangle Microwave Radiometry, **IEEE T GEOSCI REMOTE**, VOL. 45,
922 NO. 7, JULY 2007, DOI: 10.1109/TGRS.2006.888434, 2007.

923 Engelbart, D., W. Monna, J. Nash: Integrated Ground-Based Remote-Sensing Stations for
924 Atmospheric Profiling, **COST Action 720 Final Report**, EUR 24172,
925 https://doi.org/10.2831/10752, 2009.
926 Görsdorf, U., and V. Lehmann: Enhanced Accuracy of RASS-Measured Temperatures Due to an
927 Improved Range Correction. **J ATMOS OCEAN TECH**, **17 (4)**, 406–416,
928 https://doi.org/10.1175/1520-0426(2000)017<0406:EAORMT>2.0.CO;2, 2000.
929 Han, Y., and E. R. Westwater: Remote sensing of tropospheric water vapor and cloud liquid
930 water by integrated ground-based sensors. **J ATMOS OCEAN TECH**, **12**, 1050-1059, DOI:
931 https://doi.org/10.1175/1520-0426(1995)012<1050:RSOTWV>2.0.CO;2, 1995.
932 Hewison, T.: 1D-VAR Retrieval of Temperature and Humidity Profiles From a Ground-Based
933 Microwave Radiometer, **IEEE T GEOSCI REMOTE**, **45(7)**, 2163–2168,
934 https://doi.org/10.1109/TGRS.2007.898091, 2007.
935 Horst, T. W., S. R. Semmer, and I. Bogoev: Evaluation of Mechanically-Aspirated
936 Temperature/Relative Humidity Radiation Shields, 18th Symposium on Meteorological
937 Observation and Instrumentation, AMS Annual Meeting, New Orleans, LA, 10-15
938 January 2016, https://ams.confex.com/ams/96Annual/webprogram/Paper286839.html,
939 2016.
940 Kaimal, J. C., and J. E. Gaynor: The Boulder Atmospheric Observatory. **J CLIM APPL METEOROL**,
941 **22**, 863–880, https://doi.org/10.1175/1520-0450(1983)022<0863:TBAO>2.0.CO;2, 1983.
942 Küchler, N., D. D. Turner, U. Löhnert,and S. Crewell: Calibrating ground-based microwave
943 radiometers: Uncertainty and drifts, **RADIO SCI**, **51**, 311–327,
944 doi:10.1002/2015RS005826, 2016.

945 Löhnert U. and O. Maier: Operational profiling of temperature using ground-based microwave
946 radiometry at Payerne: prospects and challenges. **ATMOS MEAS TECH**, **5**, 1121–1134,
947 https://doi.org/10.5194/amt-5-1121-2012, 2012.
948 Lundquist, J. K., J. M. Wilczak, R. Ashton, L. Bianco, W. A. Brewer, A. Choukulkar, A. Clifton, M.
949 Debnath, R. Delgado, K. Friedrich, S. Gunter, A. Hamidi, G. V. Iungo, A. Kaushik, B.
950 Kosović, P. Langan, A. Lass, E. Lavin, J. C.-Y. Lee, K. L. McCaffrey, R. K. Newsom, D. C.
951 Noone, S. P. Oncley, P. T. Quelet, S. P. Sandberg, J. L. Schroeder, W. J. Shaw, L. Sparling,
952 C. St. Martin, A. St. Pe, E. Strobach, K. Tay, B. J. Vanderwende, A. Weickmann, D. Wolfe,
953 and R. Worsnop: Assessing state-of-the-art capabilities for probing the atmospheric
954 boundary layer: the XPIA field campaign. **B AM METEOROL SOC**, **98**, 289–314,
955 https://doi.org/10.1175/BAMS-D-15-00151.1, 2017.
956 Maahn, M., D. D. Turner, U. Löhnert, D. J. Posselt, K. Ebell, G. G. Mace, and J. M. Comstock:
957 Optimal estimation retrievals and their uncertainties: What every atmospheric scientist
958 should know. **B AM METEOROL SOC**, **101**, E1512-E1523, https://doi.org/10.1175/BAMS-
959 D-19-0027.1, 2020.
960 Maddy, E. S. and C. D. Barnet: Vertical Resolution Estimates in Version 5 of AIRS Operational
961 Retrievals. **IEEE T GEOSCI REMOTE**, VOL. **46**, NO. 8, AUGUST 2008,
962 https://doi.org/10.1109/TGRS.2008.917498, 2008.
963 Martinet, P., A. Dabas, J.-M. Donier, T. Douffet, O. Garrouste, and R. Guillot: 1D-Var
964 temperature retrievals from microwave radiometer and convective scale model, **TELLUS**
965 **A**, **67:1**, https://doi.org/10.3402/tellusa.v67.27925, 2015.

966 Martinet, P., D. Cimini, F. Burnet, B. Ménétrier, Y. Michel, and V. Unger: Improvement of
967 numerical weather prediction model analysis during fog conditions through the
968 assimilation of ground-based microwave radiometer observations: a 1D-Var study,
969 **ATMOS MEAS TECH**, **13**, 6593–6611, https://doi.org/10.5194/amt-13-6593-2020, 2020.
970 May, P. T. and J. M. Wilczak: Diurnal and Seasonal Variations of Boundary-Layer Structure
971 Observed with a Radar Wind Profiler and RASS. **MON WEATHER REV**, **121**, 673–682,
972 https://doi.org/10.1175/1520-0493(1993)121<0673:DASVOB>2.0.CO;2, 1993.
973 Masiello, G., C. Serio, and P. Antonelli: Inversion for atmospheric thermodynamical parameters
974 of IASI data in the principal components space. **Q J ROY METEOR SOC**, **138**, 103–117,
975 https://doi.org/10.1002/qj.909, 2012.
976 Merrelli, A. M., and D. D. Turner: Comparing information content of upwelling far infrared and
977 midinfrared radiance spectra for clear atmosphere profiling. **J ATMOS OCEAN TECH**, **29**,
978 510–526, https://doi.org/10.1175/JTECH-D-11-00113.1, 2012.
979 Neiman, P. J., D. J. Gottas, and A. B. White: A Two-Cool-Season Wind Profiler–Based Analysis of
980 Westward-Directed Gap Flow through the Columbia River Gorge. **MON WEATHER REV**,
981 **147**, 4653-4680, https://doi.org/10.1175/MWR-D-19-0026.1, 2019.
982 North, E. M., A. M.Peterson, and H. D. Parry: RASS, a remote sensing system for measuring low-
983 level temperature profiles. **B AM METEOROL SOC**, **54**, 912–919, 1973.
984 Payne, V. H., J. S. Delamere, K. E. Cady-Pereira, R. R. Gamache, J.-L. Moncet, E. J. Mlawer, and S.
985 A. Clough: Air-broadened half-widths of the 22- and 183-GHz water-vapor lines. **IEEE T**
986 **GEOSCI REMOTE**, **46**, 3601-3617, https://doi.org/10.1109/TGRS.2008.2002435, 2008.

987 Payne, V. H., E. J. Mlawer, K. E. Cady-Pereira, and J.-L. Moncet: Water vapor continuum
988 absorption in the microwave. **IEEE T GEOSCI REMOTE**, **49**, 2194-2208,
989 https://doi.org/10.1109/TGRS.2010.2091416, 2011.
990 Rodgers, C. D.: Inverse Methods for Atmospheric Sounding: Theory and Practice. Series on
991 Atmospheric, Oceanic and Planetary Physics, Vol. 2, World Scientific, 238 pp, 2000.
992 Rosenkranz, P. W.: Water vapour microwave continuum absorption: A comparison of
993 measurements and models. **RADIO SCI**, **33**, 919–928,
994 https://doi.org/10.1029/98RS01182, 1998.
995 Shaw, W., and Coauthors: The Second Wind Forecast Improvement Project (WFIP 2): General
996 Overview. **B AM METEOROL SOC**, **100(9)**, 1687–1699, https://doi.org/10.1175/BAMS-D-
997 18-0036.1, 2019.
998 Solheim, F., J. R. Godwin, J., and R. Ware: Passive ground-based remote sensing of atmospheric
999 temperature, water vapor, and cloud liquid profiles by a frequency synthesized
1000 microwave radiometer. **METEOROL Z**, **7**, 370–376, 1998a.
1001 Solheim F., J. R. Godwin, E. R. Westwater, Y. Han, S. J. Keihm, K. Marsh, R. Ware: Radiometric
1002 profiling of temperature, water vapor and cloud liquid water using various inversion
1003 methods. **RADIO SCI**, **33**, 393–404, https://doi.org/10.1029/97RS03656, 1998b.
1004 Stankov, B. B., E. R. Westwater, and E. E. Gossard: Use of wind profiler estimates of significant
1005 moisture gradients to improve humidity profile retrieval. **J ATMOS OCEAN TECH**, **13**,
1006 1285-1290, DOI:
1007 https://doi.org/10.1175/15200426(1996)013<1285:UOWPEO>2.0.CO;2, 1996.

1008 Strauch, R. G., D. A. Merritt, K. P. Moran, K. B. Earnshaw, and D. V. De Kamp: The Colorado
1009 wind-profiling network. **J ATMOS OCEAN TECH**, **1**, 37–49, https://doi.org/10.1175/1520-
1010 0426(1984)001<0037:tcwpn>2.0.co;2, 1984.
1011 Turner, D. D.: Improved ground-based liquid water path retrievals using a combined infrared
1012 and microwave approach. **J GEOPHYS RES-ATMOS, 112**, D15204,
1013 https://doi.org/10.1029/2007JD008530, 2007.
1014 Turner, D. D., and U. Löhnert: Information content and uncertainties in thermodynamic profiles
1015 and liquid cloud properties retrieved from the ground-based Atmospheric Emitted
1016 Radiance Interferometer (AERI). **J APPL METEOROL CLIM**, **53**, 752–771,
1017 https://doi.org/10.1175/JAMC-D-13-0126.1, 2014.
1018 Turner, D. D., and W. G. Blumberg: Improvements to the AERIoe thermodynamic profile
1019 retrieval algorithm. **IEEE J-STARS**, **12(5)**, 1339–1354,
1020 https://doi.org/10.1109/JSTARS.2018.2874968, 2019.
1021 Turner, D. D., and U. Löhnert: Ground-based Temperature and Humidity Profiling: Combining
1022 Active and Passive Remote Sensors. **ATMOS MEAS TECH**, **14**, 3033–3048,
1023 https://doi.org/10.5194/amt-2020-352, 2021.
1024 Ware R., Solheim F., Carpenter R., and Coauthors: A multi-channel radiometric profiler of
1025 temperature, humidity and cloud liquid. **RADIO SCI**, **38**, No. 4, 8079,
1026 https://doi.org/10.1029/2002RS002856, 2003.
1027 Weber, B. L., D. B. Wuertz, D. C. Welsh, and R. Mcpeek: Quality controls for profiler
1028 measurements of winds and RASS temperatures. **J ATMOS OCEAN TECH**, **10**, 452–464,
1029 https://doi.org/10.1175/1520-0426(1993)010<0452:qcfpmo>2.0.co;2, 1993.

1030 Wilczak, J. M., and Coauthors: The Second Wind Forecast Improvement Project (WFIP2):
1031 Observational Field Campaign. **B AM METEOROL SOC**, **100(9)**, 1701–1723,
1032 https://doi.org/10.1175/BAMS-D-18-0035.1, 2019.
1033 Wolfe, D. E. and R. J. Lataitis: Boulder Atmospheric Observatory: 1977–2016: The end of an era
1034 and lessons learned. **B AM METEOROL SOC**, **99**, 1345–1358,
1035 https://doi.org/10.1175/BAMS-D-17-0054.1, 2018.
1036